Lift Force Analysis for an Electrodynamic Wheel Maglev Vehicle

Colton Bruce, Matthew Grubbs, Jonathan Z. Bird

Laboratory for Magnetomechanical Energy Conversion and Control
Portland State University, Department of Electrical and Computer Engineering, Portland, OR, USA

This paper used an analytic based 3-D second order vector potential model to study the vertical dynamic force ripple and dynamic airgap height change when using a one pole-pair electrodynamic wheel (EDW) maglev vehicle. A one-pole pair EDW creates the lowest lift specific power; however transient finite element analysis (FEA) also shows that the one pole-pair EDW will create a large oscillating vertical force when maintaining a static airgap height. A dynamically coupled eddy current model was used to confirm that when the airgap length is allowed to change with time then an increase in vertical airgap creates a large decrease in lift force thereby mitigating any large oscillatory airgap height changes from being created by the one pole-pair EDW. The small airgap height variation was experimentally confirmed by using a four-wheeled proof-of-principle radial EDW maglev vehicle.

***Index Terms*— Electrodynamic wheel, lift-to-drag ratio, maglev, magnetic levitation, specific power, electric aircraft.**

I. Introduction

When a magnetic wheel is rotated over a conductive track, such as aluminum or copper, track eddy currents are induced that give rise to a levitation force [1-11]. An illustration of a one pole-pair radial and a one-pole pair axial electrodynamic wheel (EDW) is shown in Fig. 1. The radial EDW field interaction with a flat track is lower than for an axial EDW but unlike the axial EDW a single radial EDW can also create thrust when over the flat passive track. The radial EDWs field rotation is also in the same direction as the travel direction, this therefore gives rise to a relatively high thrust force.

The magnetic levitation (MagLev) vehicle configured with EDWs can create a relatively high lift-to-weight ratio from a simple passive low-cost aluminum sheet guideway and therefore the track construction costs for such a maglev vehicle will be relatively low. The utilization of a passive flat guideway could also enables the maglev technology to be integrated into existing rail infrastructure and does not require new dedicated elevated guideways to be built [12]. In addition, as the mechanical rotation of the magnets induces the track current rather than directly from current excited windings, the use of the separate drive motor shields the power supply from experiencing the adverse effects of the highly inductive track field interaction [13]. This circumventing the need for the power supply to counteract a very low power factor.

All prior published radial EDW designs [1-4, 6] utilized multi pole-pair rotors, such as four pole-pairs [1-4] and two pole-pairs [5, 6]. Using more pole-pairs improves the thrust efficiency, but due to its higher electrical frequency, it greatly increases the lift specific power (W/kg) thereby significantly increasing the total vehicle power consumption [5]. The use of a one-pole pair rotor will create the lowest specific power as well as simplify the rotor construction, since the field can be directed along one diametric magnetization direction. If multiple one pole-pair EDWs are used in series then an EDW vehicles thrust performance can be greatly improved allowing it to operate with both a low specific power and a relatively high efficiency [14]. An overview analysis of the performance benefits of using the one pole-pair EDW in a series configuration is provided in the Appendix.

The use of a one pole-pair rotor was previously thought to not be suitable for an EDW because it creates a large oscillating lift force when the airgap is fixed. This concern was highlighted in a recent paper [15] in which the authors recommended that to minimize the vertical oscillation force the number of pole-pairs should be greater than two. The purpose of this paper is to present an analytic and numerical based dynamic modelling study that shows that the use of a one pole-pair radial EDW can operate with a near constant airgap without encountering dynamic vertical oscillation issues. The stable lift performance is then experimentally verified through the testing of a four-wheeled, EDW-maglev vehicle.

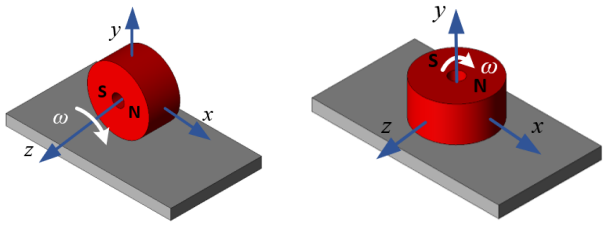

Fig. 1. An illustration of the (a) radial EDW and (b) axial EDW typology

II. Rotor Comparison

A diametrically magnetized one pole-pair EDW rotor contains magnets that are magnetization in only one direction and will create a highly sinusoidal field. The one pole-pair rotor is of interest, because for a given mechanical angular speed and radius, the one pole-pair rotor will have the lowest electrical frequency and therefore have the lowest power loss for a given amount of lift mass. This observation is confirmed in Appendix B. Fig. 2 shows three rotor designs in which the magnet segments are all magnetized along the same axis and Fig. 3 compares the field magnitudes for each of these designs. As expected, the design in which the inner rotor is $r_i = 0$, creates the largest magnitude field and the use of a ferromagnetic core will also improve the rotor field relative to the air-core design. The rotor that has $r_i = 0$ will yield the highest lift-to-weight ratio (refer to Appendix C). However, having no inner rotor radius is impractical. To study the air-gap dynamics in this paper the rotor designs shown in Fig. 2(b) and Fig. 2(c) will be used. The

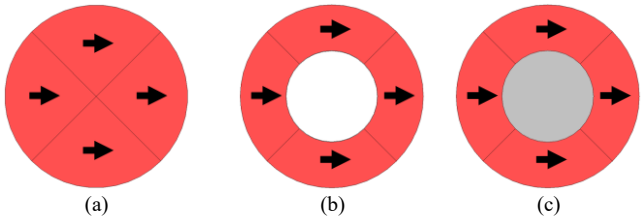

Fig. 2. Examples of different single pole-pair rotor designs. (a) shows a diametric magnetized magnet cylinder, with inner radius $r_i = 0$, (b) a diametric magnetized magnet with an inner radius $r_i = 20$mm, and (c) a diametric magnetized magnet with 1018 ferromagnetic shaft material.

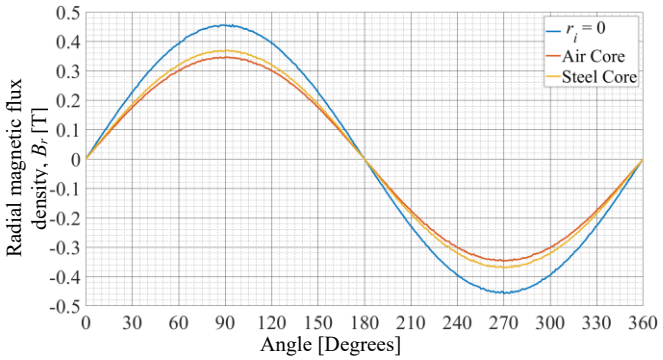

Fig. 3. (a) Comparison of the 3-D FEA calculated magnetic flux density for the case when the radius dimensions are (r_o, r_i) = (40,0) mm, (b) when (r_o, r_i) = (40,20) mm with an air-core, and (c) with (r_o, r_i) = (40,20) mm with a 1018 steel rotor core. The fields were all evaluated 10 mm above the rotor surface.

purely sinusoidal field created by these designs enable a good match to be obtained with the one-pole pair EDW analytic model [16, 17].

III. Force Ripple

A 2-D illustration of a one pole-pair EDW rotating with an angular speed ω and translating with velocity v_x is shown in Fig. 4. The induced currents created by the motion of the EDW are primarily under the EDW and travel backwards in waves within the conductive track. It is computationally challenging and very time consuming to use 3-D FEA models to compute the forces created by the EDW. To speed up simulations times this paper uses a one pole-pair EDW analytic based second order vector potential (SOVP) Fourier series modelling approach [16, 17]. The SOVP formulation is computationally useful because for cases in which the EDW rotor is centered over a very wide and long conductive track then the track length and width can be assumed to have infinite width and length [16, 17]. In this case the number of SOVP unknowns will reduce down to just one normally directed vector component. The infinite track width and track length assumption are modelled by ensuring that the width, w, and length, l, of the conduct track are sufficiently long that the field and currents are negligibly small near the ends. Appendix A shows the derivation of SOVP model with a one pole-pair EDW that is used in this paper.

When the airgap is maintained at a fixed height, $y = y_g$, the rotation of the one pole-pair EDW gives rise to a large average lift force, $F_{y,a}(y_g, \omega, v_x)$, but also a large overlayed oscillation force. In the following force ripple analysis, the translational speed, v_x, is assumed to be zero.

Fig. 5 shows an example 3-D JMAG transient FEA calculated normalized lift force plot, as a function of time, for both a one and a two pole-pair EDW. Due to the large pole-pitch created by the one pole-pair EDW the rotor will create a large oscillating force. The lift force ripple angular frequency, ω_r, is always twice the electrical rotational frequency, ω, of the EDW such that $\omega_r = 2P\omega$, where for this analysis $P = 1$ pole-pairs. Based on these FEA simulation observations the time changing lift force can be accurately described by

$$F_y(t, y_g, \omega) = F_{y,a}(y_g, \omega, 0) + F_{y,r}(y_g, \omega)\sin(2\omega t) \qquad (1)$$

where $F_{y,a}$ is the average value of the lift force, derived in Appendix A, and $F_{y,r}$ is the force ripple amplitude which was computed from the FEA model. The steady-state analytic based model cannot predict this ripple amplitude.

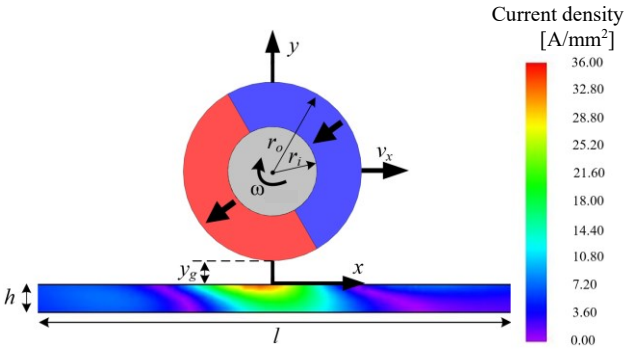

Fig. 4. A single $P = 1$ pole-pair radial EDW, the induced current density in the conductive track along with the geometric definitions are also shown.

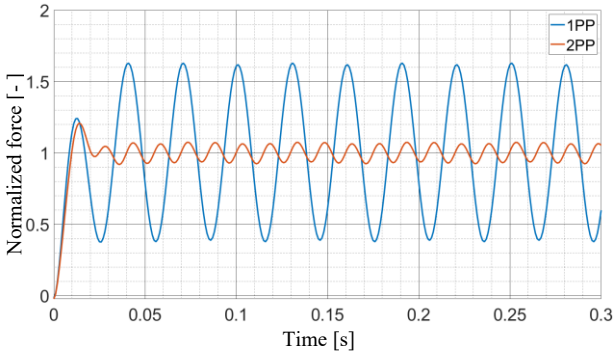

Fig. 5. A 3-D FEA transient lift force simulation plot for both a single one pole-pair and a two pole-pair EDW rotating at $\omega = 1000$ r/min. The airgap was fixed at $y_g = 10$ mm and the translational speed v_x is zero. The experimental values shown in Table I were used to create this figure. The same rotor dimensions were used for both the one and two pole pairs.

TABLE I. Steady-State Modelling and Experimental Prototype Parameters

Model	Experimental	Steady-state model	Units
Pole-pairs, P	1	1	-
Outer radius, r_o	12.7	40	mm
Inner radius, r_i	3.175	14.8	mm
Rotor width	$2\times r_o$	70	mm
Residual flux density, B_{rm}	1.32	1.42	T
Relative permeability, μ_r	1.05	1.055	-
Vehicle mass, m	1.687	-	kg
Track thickness, h	12.7 ± 0.23	10	mm
Track width, w	88.9	200	mm
Track length, l	300	1200	mm
Track conductivity	2.46×10^7	5.69×10^7	S/m

The lift force ripple amplitude ratio defined by:

$$\Gamma_y(\omega) = \frac{F_{y,r}(y_g,\omega)}{F_{y,a}(y_g,\omega,0)} \quad (2)$$

is constant with respect to the airgap, y_g, and only changes with angular speed. Therefore, when the angular speed is fixed, (2) can be substituted into (1) giving the time changing lift force in which only the average force is a function of airgap:

$$F_y(y_g,\omega,t) = F_{y,a}(y_g,\omega,0)[1+\Gamma_y(\omega)\sin(2P\omega t)] \quad (3)$$

Fig. 6 shows how the lift force ripple amplitude ratio decreases as the angular speed increases. The experimental values shown in Table I were used to create this plot. It should be noted that the rotor radius and width also affect the force ripple amplitude. When using the experimental values given in Table I the lift force ripple amplitude can be accurately curve fit by using:

$$\Gamma_y(\omega) = 132 - 0.01\omega + \left(4.8\times10^{-5}\right)\omega^2 - \left(1.2\times10^{-8}\right)\omega^3 + \left(1.2\times10^{-12}\right)\omega^4 . \quad (4)$$

To investigate the impact of the force change with airgap the 1-D non-linear magnetic spring damper model, shown in Fig. 7, was developed. The change in airgap can be described by

$$m\frac{d^2y_g}{dt^2} + c_{yy}(y_g,\omega)\frac{dy_g}{dt} - k_{yy,t}(y_g,\omega,t)\cdot y_g + mg = 0 \quad (5)$$

where m = mass of system, g = gravitational constant, c_{yy} = vertical eddy current damping term and $k_{yy,t}$ = stiffness function. For simulation purposes the eddy current damping is assumed to not change with time but the stiffness change with time must be accurately accounted for, and was determined by taking the derivative of (3). This gives

$$k_{yy,t}(y_g,\omega,t) = k_{yy}(y_g,\omega)[1+\Gamma_y(\omega)\sin(2\omega t)] \quad (6)$$

where the EDW magnetic spring constant, k_{yy}, as a function of airgap and angular speed is

$$k_{yy}(y_g,\omega) = -\frac{\partial F_{y,a}(y_g,\omega,0,0)}{\partial y_g} \quad (7)$$

The eddy current stiffness and damping equations used in (5) are derived in Appendix A. The change in the stiffness and damping as a function of airgap height and angular speed for a single EDW rotor is shown in Fig. 8. The experimental values shown in Table I were used to create these plots. Fig. 8 shows that the eddy current damping is very small, and this will result in a long simulation time, therefore, to enable the model to reach a steady-state within a reasonable simulation time a fixed arbitrary damping term defined by c_{yy} = 100 Ns/m was used in (5) to speed up the simulation time. Since the damping does affect the magnitude of the final steady-state oscillation airgap change the analysis conclusions will be unchanged [18].

A Matlab-Simulink representation of the 1-D EDW spring-mass damper system is shown in Fig. 9. A look-up table based on the lift force plot shown in Fig. 10 was used to compute the steady-state lift force $F_{y,a}$. The steady-state time changing airgap variation and lift force when the input angular speed is ω= 3000 r/min is shown in Fig. 11. Note that these results are at the operating condition when the angular speed is not changing.

Fig. 11 shows that whilst the lift force variation is large the airgap height change is minuscule. Due to the large magnetic stiffness as the airgap begins to decrease the lift force increases significantly thereby counteracting any large changes in airgap. The inertia of the rotor is also sufficiently large that the change in momentum of the vehicle over the short high and low force periods is sufficiently low to not significantly change the average airgap height value. The peak-to-peak airgap amplitude cha-

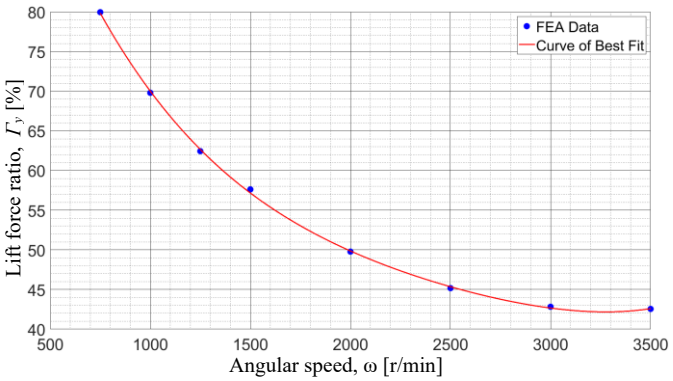

Fig. 6. 3-D FEA calculated force ripple amplitude ratio, Γ_y at different angular rotational speeds. The ratio does not change with different airgap heights.

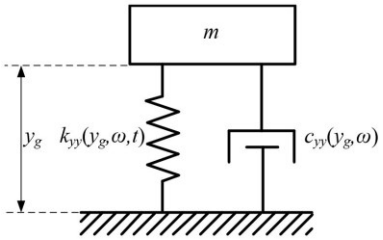

Fig. 7. 1-D model of the EDW maglev system.

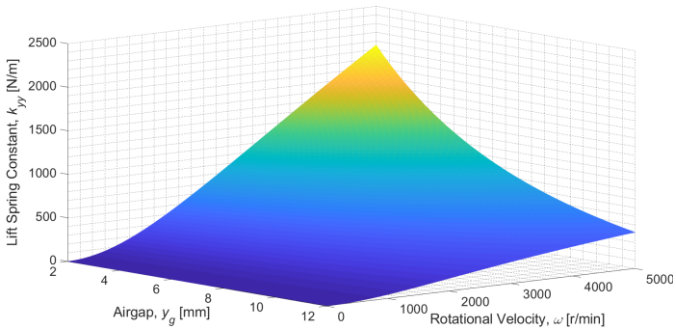

(a)

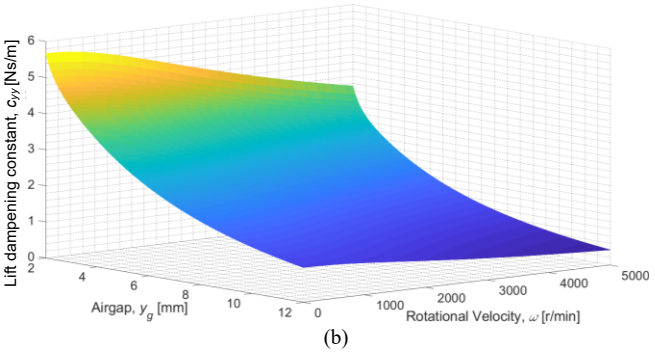

(b)

Fig. 8. (a) Vertical spring constant, k_{yy} and vertical damping, c_{yy}, change as a function of angular speed and airgap height for an individual rotor

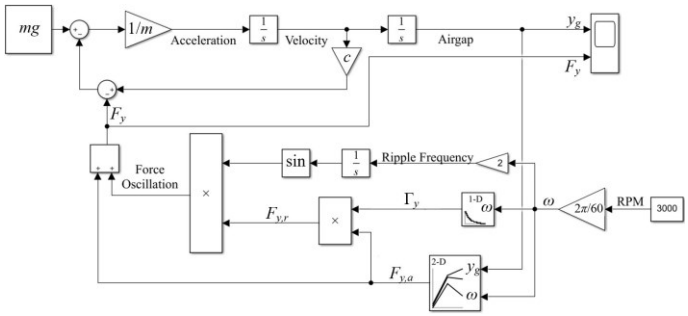

Fig. 9. A one dimensional Matlab-Simulink EDW lift force dynamic spring model when ω = 3000 r/min.

nge is only Δy_g = 0.021 mm, or 0.3%, of the average airgap height y_g = 7.095mm, this is well within a reasonable tolerance limit. To put this airgap variation in perspective, this variation is less than the ± 0.05 mm surface variation tolerance of the aluminum sheets that were used in the experimental setup.

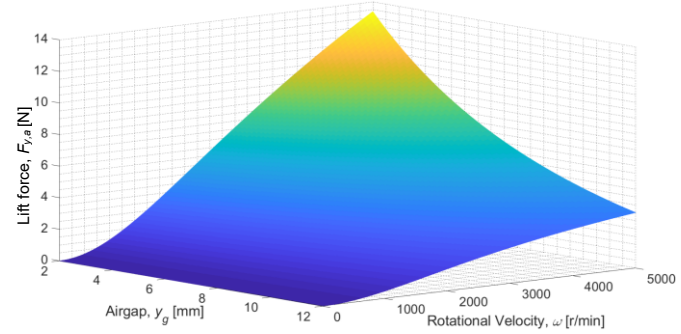

Fig. 10. Lift force change with respect to airgap height, y_g, and angular speed, ω, for an individual rotor.

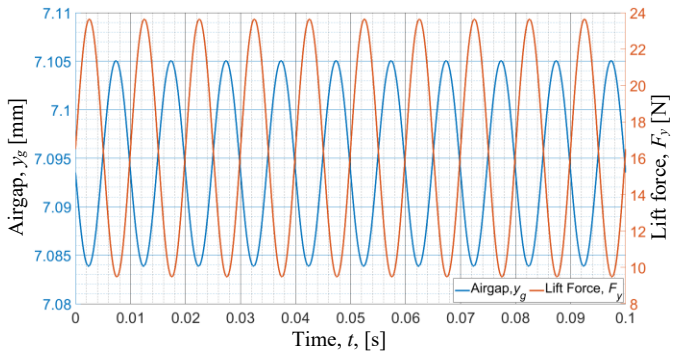

Fig. 11. Example oscillating airgap and the corresponding lift force for a single one pole pair EDW rotating at 3000 r/min when modeled using an equivalent spring. The analysis parameters shown in Table I were used.

IV. EDW Maglev Vehicle Airgap Measurement

To experimentally verify the small vertical oscillations that are created by a one pole-pair EDW a low-cost laboratory scale EDW maglev vehicle was built that contained four one pole-pair EDW rotors. The geometric parameters used in the sub-scale experimental setup are shown in Table I. and a front and top view of the EDW maglev vehicle is shown in Fig. 12.

A carbon fiber base was used for the body of the EDW vehicle with 3-D printed motor mounting brackets attached to secure the magnet rotors. The EDW rotors were driven using a brushless DC motor (model Prop-drive 28-30 with k_v = 800 rpm/V). The mounting brackets were constructed such that the magnet rotors sat 2.1mm above the 12.7mm thick aluminum track when at rest. The brushless DC motors were sensorlessly controlled by using a DYS Aria 35A electronic speed controller with an Arduino Mega 2560 controller. Four 3.7V, 7.4Wh Li-ion batteries (model number 18650) were used to provide power to the motor's sensors. Each EDW rotor airgap height was measured by using a Panasonic HL-G105-S-J laser displacement sensor (± 0.01mm accuracy). All the vehicle horizontal movements, with respect to the aluminum track, were eliminated by affixing a pair of roller ball bearing brackets on each side of the track. The roller balls allowed for unhindered vertical movement, while inhibiting horizontal and lateral vehicle movement.

To verify that the lift force ripple has marginal effect on maintaining a stable airgap the EDW vehicle was operated at ω = 3000 r/min. Fig. 13(a) shows the motors' angular speed and Fig. 15(b) shows the corresponding rotor airgaps as a function of time. As the vehicle lifted off the rotors reach a steady-state operating airgap height at time $t \approx$ 2.3s. Due to the low-cost components used in this proof-of-principle demonstration the speed values obtained and set points defined were limited by the speed measurement resolution and sampling time; the calculated angular speed step-size resolution was 16 r/min. The

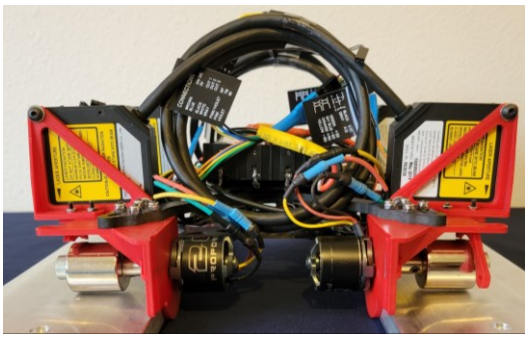

(a)

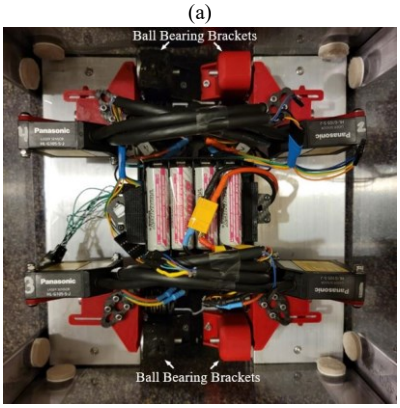

(b)

Fig. 12. (a) Front view and (b) top view of the four EDW rotor maglev drone. The proof-of-principle EDW maglev drone was placed above a 6061-grade aluminum dual-track. The aluminum is 12.7 mm thick and 88.9 mm wide each. The EDW maglev drone was contained within a support box and horizontally stabilizing by using ball bearing brackets that allowed the maglev vehicle to move freely vertically.

angular speed and airgap performance could be further improved by increasing the control performance. Currently, the controller sampling period is near that of the rotor rotational period for the range of angular speeds in which the maglev vehicle operated, ranging between 18 ms to 20 ms. This slow sampling speed is primarily attributed to limitations in the communication and processing speeds between the low-cost Arduino

Mega 2560 and the laser displacement sensors that were selected for this proof-of principle demonstration. Despite the presence of the poor speed control, Fig. 13 shows that the measured airgap height is remarkably stable. The measured airgap of the forward section of the maglev vehicle (rotors 1 and 3) are 0.5mm lower than the rear section. This change in airgap height is illustrated in Fig. 14 and the pitch angle for the vehicle was computed by evaluating

$$\theta_z \cong \frac{y_3 + y_1 - y_4 - y_2}{4l_v} \tag{8}$$

where l_v =half-length between rotors. Fig. 15 shows the measured pitch angle as a function of time. The angle variation is very small. The vehicle is pitched because of non-uniform vehicle weight distribution Table II shows a comparison of the average airgap and peak-to-peak airgap variation between the spring model and measured value of each rotor. While the average measured airgap values are not equal, the peak-to-peak variation does not exceed 0.1 mm, or 1.3% of the airgap, for any

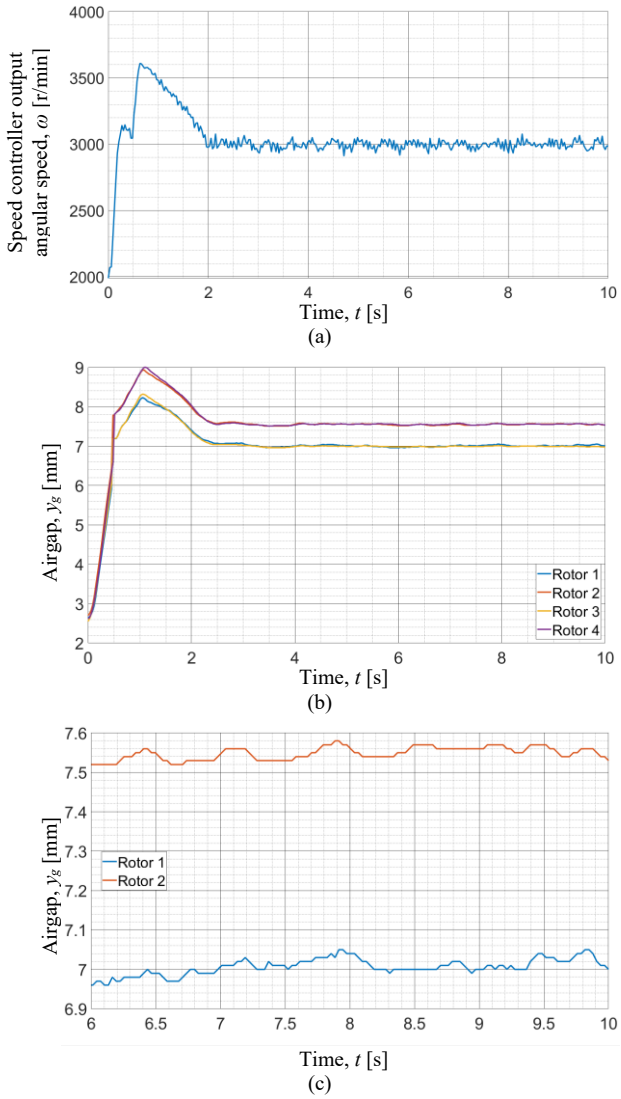

Fig. 13.(a) Experimentally measured drone rotor angular speed on one rotor, (b) measured rotor airgap, and (c) zoomed in view of rotor 1 and 2 airgaps when trying to maintain ω = 3000 r/min. The angular speed value is reported by the motor controller.

TABLE II. SIMULATED MODEL AND MEASURED ROTOR AIRGAP COMPARISON

Model		Average Airgap [mm]	Peak-to-peak Variation [mm]	% Variation
Matlab Simulink		7.10	0.02	0.28
Measured Airgap for	Rotor 1	7.01	0.09	1.28
	Rotor 2	7.55	0.06	0.79
	Rotor 3	6.99	0.04	0.57
	Rotor 4	7.55	0.05	0.66

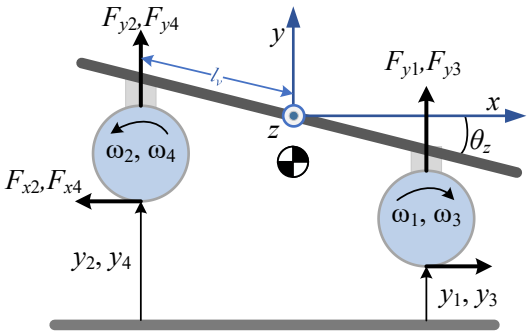

Fig. 14. Rotor force definitions and pitch angle, θ_z, definition for the maglev drone,

of the rotors. The small increase in measured average airgap height variation relative to the simulated value is likely due to a combination of experimental factors, such as variations in the track surface height, slight flexing of the EDW vehicle frame and motor mounting brackets, as well as imbalance in the weight distribution of the vehicle. Note that the friction in the roller bearings was not accounted for in the modelling.

With the steady operation confirmed to be achievable for a desired angular speed, even in the presence of the large force ripple, an airgap height control was implemented, the direct control of the rotor heights was maintained at a specified airgap by changing the angular speed.

Fig. 15 shows the measured airgap and rotor angular speeds of the maglev vehicle when the desired airgap and pitch of y_g = 7 mm and θ_z = 0 was defined for all rotors. Fig. 15 shows that even in the presence of poor RPM control, attributed to the reasons stated above, the performance of the system's airgap, and pitch, is good, with an average airgap of y_g = 7 mm being achieved and a peak-to-peak variation for each rotor that does not exceed 0.32 mm.

CONCLUSION

The one pole-pair EDW creates the lowest lift specific power, but it also creates a large oscillating lift force. By using a dynamic eddy current model along with an experimental EDW maglev vehicle this paper confirms that the presence of a large oscillatory lift force does not result in a large steady-state oscillating airgap height. This is because as the lift force decreases the airgap height also decreases and even a small airgap reduction greatly increases the lift force thereby counteracting the varying lift force magnitude. A proof-of-principle EDW vehicle simulation showed that when the average airgap was maintained at y_g = 7.095mm the measured EDW vehicle peak-to-peak airgap amplitude change was only 0.021 mm. This paper also presented a new 4 rotor EDW-maglev vehicle and experi-

mentally demonstrated that the vehicle can operate with a minimal airgap oscillation. The use of a low-cost speed control was implemented on the EDW vehicle and a peak-to-peak airgap height variation of less than 0.1 mm was measured. Further dynamic modelling with respect to resonance mitigation and stability when travelling is still needed.

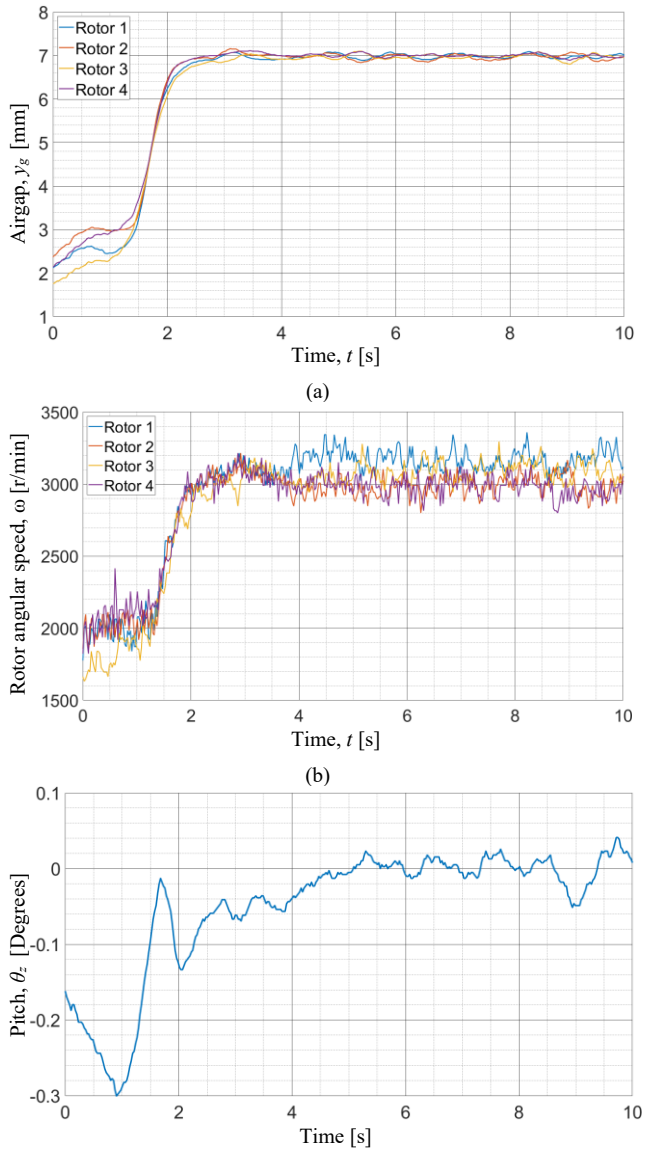

Fig. 15.(a) Measured EDW vehicle rotor airgap, (b) rotor RPM when set to maintain rotor heights at 7 mm, (c) vehicle pitch.

ACKNOWLEDGEMENTS

The authors would like to thank the JMAG Corporation for the use of their finite element analysis software. This material is based upon work supported by the National Science Foundation under grant number 1810489.

APPENDIX

A. *Summary of Analytic Based EDW Model*

A complex Fourier series-based SOVP EDW rotor formulated presented in [16, 17] solved the governing steady-state 2nd order partial differential equations by summing up the spatial harmonic field components along an *x*-*z*-axis. The axis definitions for the model are shown in Fig. 4. The *n*th and *m*th Fourier harmonic component wavenumber along the *x*- and *z*-axis are respectively defined as:

$$\xi_m = 2\pi m/l \tag{9}$$

$$k_n = 2\pi n/w \tag{10}$$

The 3-D magnetic rotor source field was calculated directly from the field created by an equivalent fictitious magnetic charge cylinder [19, 20]. The B_y component source field is normally directed into the conductive track and for a Halbach rotor with P pole-pairs can be accurately modeled in 3-D by evaluating:

$$B_y^{so}(x,y,z,t) = \frac{B_r r_o e^{-jP\omega t}}{2\pi}\int_0^{2\pi}\int_{-w_o/2}^{w_o/2}\frac{e^{jP\theta_o}}{R^3}(y-y_c-r_o\sin\theta_o)dz_o d\theta_o \tag{11}$$

where

$$B_r = \frac{2B_{res}P(1+\mu_r)(r_i^{P+1}-r_o^{P+1})r_o^{2P}}{(1+P)[(1-\mu_r)^2 r_i^{2P}-(1+\mu_r)^2 r_o^{2P}]}\frac{1}{r_o^{P+1}} \tag{12}$$

$$R=[(x-x_c-r_o\cos\theta_o)^2+(y-y_c-r_o\sin\theta_o)^2+(z-z_c-z_o)^2]^{1/2} \tag{13}$$

and B_{res} = residual flux density, μ_r = magnet relative permeability. The Halbach rotor origin is located at (x_c, y_c, z_c) = $(0, r_o+y_g, 0)$. Interestingly (12) is still valid for P =1 pole-pairs, in which case (12) reduces down to

$$B_r = B_{res}\frac{(1+\mu_r)(r_i^2-r_o^2)}{[(1-\mu_r)^2 r_i^2-(1+\mu_r)^2 r_o^2]} \tag{14}$$

The complex exponential term in (11) was used to model the field rotation of the Halbach rotor in steady-state [16, 20]. To couple the source field with the conductive plate and form term-by-term mode matching the source must be put into a Fourier harmonic form. The Fourier harmonic field at the surface of the conductor is

$$B_y^s(x,y_g,z,t) = \sum_{m=-\infty}^{\infty}\sum_{n=-\infty}^{\infty} S_{mn}e^{j\xi_m x}e^{jk_n z}e^{-jP\omega t} \tag{15}$$

where the complex harmonic magnitude terms in (15) are determined by evaluating (11), such that [19, 20]

$$S_{mn} = \frac{1}{lw}\int_{-w/2}^{w/2}\int_{-l/2}^{l/2} B_y^{so}(x,y_g,z,t)e^{-j\xi_m x}e^{-jk_n z}dxdz \tag{16}$$

The integration of (11) with respect to z_o was performed analytically whereas the integration with respect to θ_o was numerically evaluated.

To study the oscillating lift force in this paper the radial EDW is assumed to induce currents through both the angular rotation and vertical motion, v_y. These motions create eddy currents in the conductive track that create a reflected steady-state eddy current field that is described by [16, 20]

$$\mathbf{B}^r(x,y,z,t) = -j\sum_{m=-\infty}^{\infty}\sum_{n=-\infty}^{\infty} S_{mn}R_{mn}[\xi_m\hat{x}+j\kappa_{mn}\hat{y}+k_n\hat{z}] \times\frac{1}{\kappa_{mn}}e^{-\kappa_{mn}(y+y_g)}e^{j\xi_m x}e^{jk_n z}e^{-jP\omega t} \tag{17}$$

where R_{mn} is the unitless reflection coefficient given by [16, 20]

$$R_{mn} = \frac{\mu_0\sigma\left(\kappa_{mn}v_y + jP\omega\right)}{2\kappa_{mn}^2 - j\mu_0\sigma P\omega + 2\kappa_{mn}\beta_{mn}\coth(\beta_{mn}h)} \tag{18}$$

$$\beta_{mn}^2 = \frac{1}{4}(v_y \mu_0 \sigma)^2 + \kappa_{mn}^2 - j\mu_0 \sigma P \omega \tag{19}$$

$$\kappa_{mn}^2 = \xi_m^2 + k_n^2 \tag{20}$$

where σ = track conductivity and h = track thickness. The force created by the induced eddy current field interacting with the radial EDW source field can be computed by utilizing Maxwell stress tensor in the form:

$$\mathbf{F} = \frac{1}{2\mu_0} \int_{-l/2}^{l/2} \int_{-w/2}^{w/2} B_y^s(x, y_g, z)^* \mathbf{B}^r(x, y_g, z) dx dz \tag{21}$$

where the superscript star denotes complex conjugation. Note that the half term in (21) does not appear like in other force equations and this is due to the field functions being complex. When the rotor has an airgap, y_g, the steady-state average thrust, $F_{x,a}$, and average lift force, $F_{y,a}$, components can be calculated by evaluating

$$F_{x,a}(y_g, \omega, v_x) = -\frac{wl}{\mu_0} \sum_{m=-M}^{M} \sum_{n=-N}^{N} \left|S_{mn}\right|^2 e^{-2\kappa_{mn} y_g} \frac{\xi_m}{\kappa_{mn}} \mathrm{Im}\left\{R_{mn}(\omega, v_y)\right\} \tag{22}$$

$$F_{y,a}(y_g, \omega, v_x) = -\frac{wl}{\mu_0} \sum_{m=-M}^{M} \sum_{n=-N}^{N} \left|S_{mn}\right|^2 e^{-2\kappa_{mn} y_g} \mathrm{Re}\left\{R_{mn}(\omega, v_y)\right\} \tag{23}$$

Substituting (22) into (7) and evaluating gives

$$k_{yy}(y_g, \omega) = -\frac{2wl}{\mu_0} \mathrm{Re}\left\{ \sum_{m=-M}^{M} \sum_{n=-N}^{N} \left|S_{mn}^y\right|^2 e^{-2\kappa_{mn} y_g} R_{mn}(0) \kappa_{mn} \right\} \tag{24}$$

The vertical eddy current damping is described by

$$c_{yy}(y_g, \omega) = -\frac{\partial F_{y,a}(y_g, \omega, 0)}{\partial v_y} \tag{25}$$

Evaluating (25) gives:

$$c_{yy}(y_g, \omega) = \frac{wl}{\mu_0} \mathrm{Re}\left\{ \sum_{m=-M}^{M} \sum_{n=-N}^{N} \left|S_{mn}^y\right|^2 e^{-2\kappa_{mn} y_g} \frac{\partial R_{mn}}{\partial v_y} \right\} \tag{26}$$

The steady-state model parameters for a one pole-pair EDW rotor, as defined in Table I were used to validate the analytic based model. The JMAG FEA model and analytic based lift and thrust force comparison is shown in Fig. 16. The analytic based forces given by (22) and (23) were numerically evaluated by using (N, M) = (64, 256) spatial harmonic terms. Fig. 16 shows that a sufficiently accurate agreement between the data was obtained. The error is smaller when the forces are higher, and this is believed to be due to the limitation in the mesh size used.

When the EDW angular rotational speed ω is greater than the translational speed v_x a positive slip speed is created. The EDW slip speed is defined by

$$s_l = \omega r_o - v_x \tag{27}$$

A positive slip gives rise to a thrust force, and larger braking forces are created when the slip speed is negative. Using the one pole-pair EDW steady-state parameters, as shown in Table I, an example of the lift and thrust force change with slip and translational speed is shown in Fig. 17 (a) and (b).

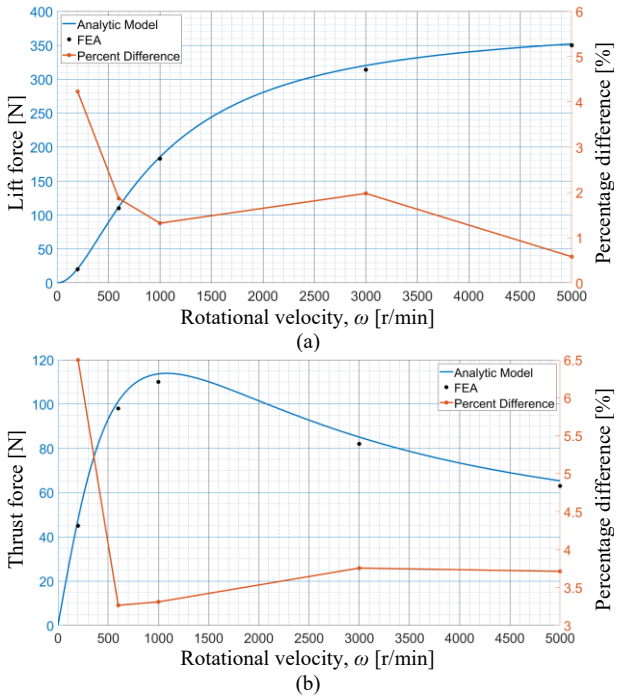

Fig. 16. (a) Lift and (b) thrust force comparison between the FEA model and analytic model, with percentage difference between models.

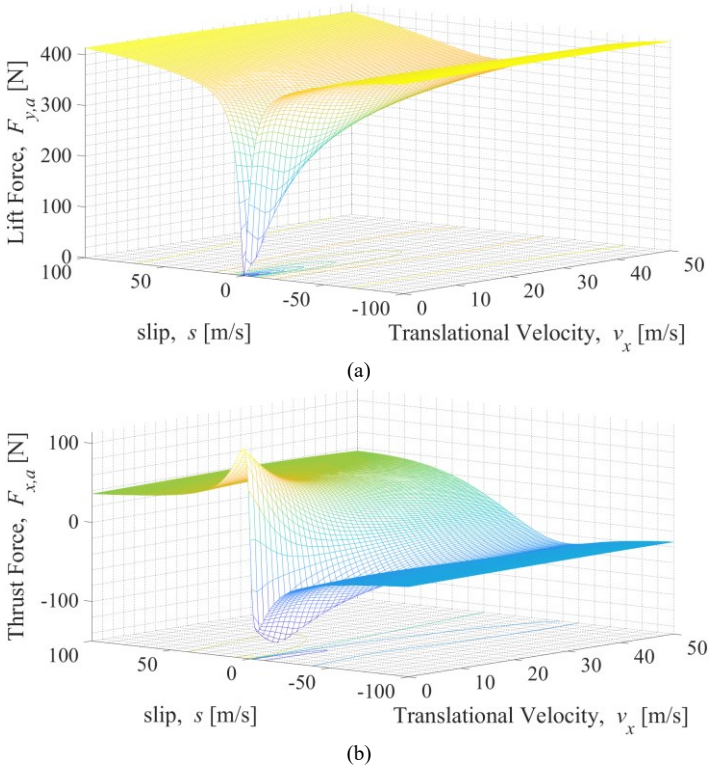

Fig. 17. (a) Illustration of how the average lift force and (b) thrust force change with slip speed and translational speed, v_x. The analysis model parameters shown in Table I were used to compute the force.

B. *Specific Power*

The lift performance for an EDW can be compared by computing the lift specific power, which defines the power-per-kilogram required to support the vehicle:

$$S_w = \frac{P_L(y_g, \omega, v_x)}{F_{y,a}(y_g, \omega, v_x)/g} \quad \text{[W/kg]} \qquad (28)$$

where P_L is the power loss within the conductive track, F_y is the lift force, and g is acceleration due to gravity. Both the power loss and lift force in (28) are shown as a functions of the airgap, translational speed v_x and EDW slip speed s_l.

Using the parameters shown in Table I the analytic-based SOVP model presented in the Appendix was used to compute the lift specific power for different radii and pole-pair numbers, and example specific power loss plot is shown in Fig. 18 and it confirms that the lowest lift specific power will occur when the lowest number of rotor pole-pairs is used.

C. *Lift-to-Weight Ratio Comparison*

Using the steady-state parameters shown in Table I. The lift-to-weight ratio, for the one pole pair EDW was analytically evaluated as a function of inner rotor radius for the case when (ω, v_x) = (3000 r/min, 10 m/s). The lift-to-weight ratio is defined as

$$L_w = \frac{F_{y,a}(y_g, \omega, v_x)}{m_e g} \qquad (29)$$

where F_L = lift force, m_e = rotor mass. Fig. 19 confirms that the highest lift-to-weight ratio, occurs when the inner radius is zero.

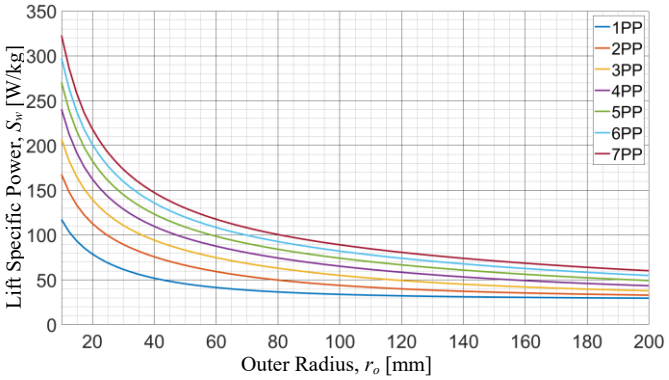

Fig. 18. Lift specific power comparison between different rotor pole-pair counts over a range of rotor outer radius values, a lower showing smaller pole-pair numbers resulting in relatively reduced lift specific power. EDW system simulated parameters are given in Table III

TABLE III. LIFT SPECIFIC POWER SIMULATION PARAMETERS

Model	Steady-state model	Units
Pole-pairs, P	[1,2,3,4,5,6,7]	-
Outer radius, r_o	10 to 200	mm
Inner radius, r_i	r_o[0, 0.37, 0.575, 0.684, 0.746, 0.79, 0.82]	mm
Rotor width	$2r_o$	mm
Residual flux density, B_{rm}	1.42	T
Relative permeability, μ_r	1.055	-
Translational Velocity, v_x	25	m/s
Slip speed, s_l	40	m/s
Track thickness, h	10	mm
Track conductivity	5.69×10^7	S/m

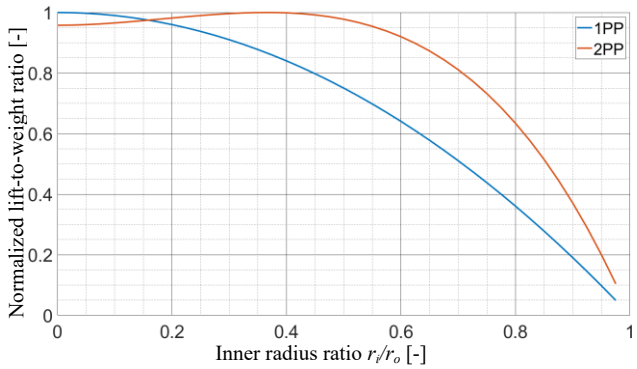

Fig. 19. (a) Normalized lift-to-weight ratio as a function of inner radius ratio for a one and two pole-pair rotor. Lift force computed for case when (v_x, ω) = (3000 r/min, 10 m/s).

D. *Efficiency*

The EDW thrust efficiency is defined as:

$$\eta = \frac{F_x(y_g, \omega, v_x) \cdot v_x}{F_x(y_g, \omega, v_x) \cdot v_x + P_L(y_g, \omega, v_x)} \qquad (30)$$

It was shown in [5, 14] that when using a single EDW the higher the pole-pair number the higher the thrust efficiency. However, Fig. 18 showed that the use of a high number of pole-pairs negatively impacts the lift specific power. A single one pole-pair EDW will therefore always have the lowest lift-specific power, but also a low thrust efficiency.

To greatly improve thrust efficiency multiple one pole-pair EDW in series can be used thereby allowing an EDW-maglev to operate with the lowest lift specific power whilst also providing good thrust efficiency. For example, the improvement in the lift and thrust as a function of numbers of rotors in series is shown in Fig. 20. The parameters used to create this plot are shown in Table IV. The rotor spacing was set to equal the rotor radius. Each consecutive rotor has a relative phase shift of 180°, thereby allowing the following EDW to take advantage of the induced track field from the proceeding EDW. The improvement in thrust efficiency along with the reduction in lift specific power, as a function of rotors in series, is shown in Fig. 21. Fig. 21 shows that the thrust efficiency can be doubled if using four EDW in series and the lift-specific power is also reduced. Fig. 21(c) does show a decrease in the lift-to-weight ratio, however, a good lift-to-weight ratio, ≥ 8, can still be obtained when the slip is increased. It should be noted that the lift specific power values shown in Fig. 21 are relatively high because the radius used in this example study was very small.

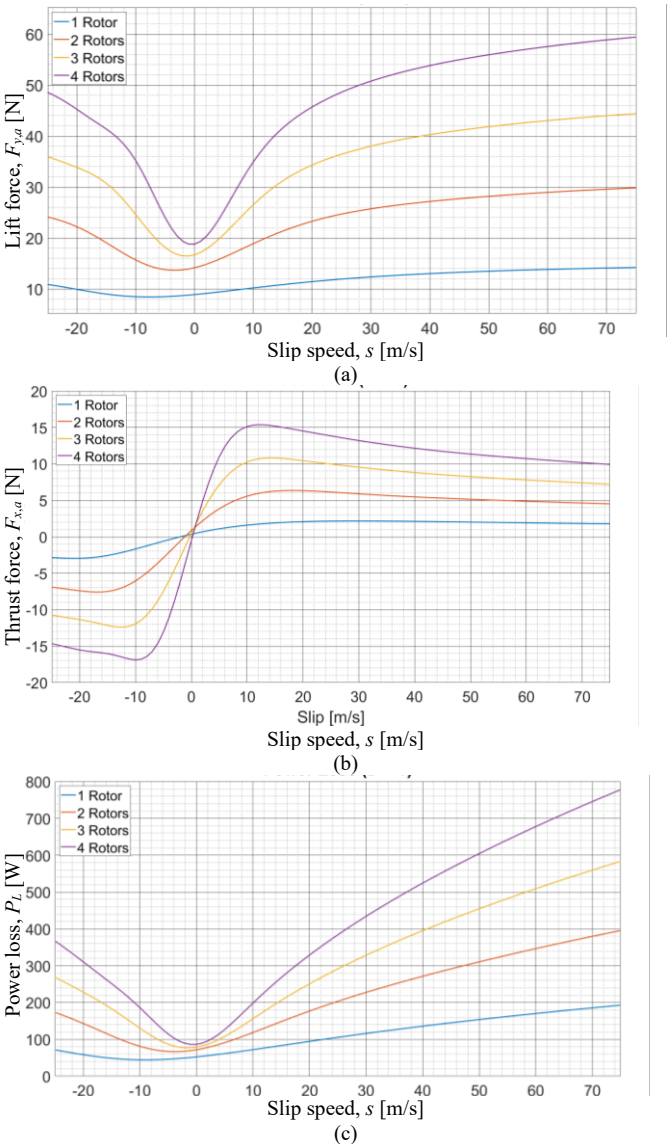

Fig. 20. Example calculation showing the (a) lift, (b) thrust and (c) power loss change when using multiple rotors in series.

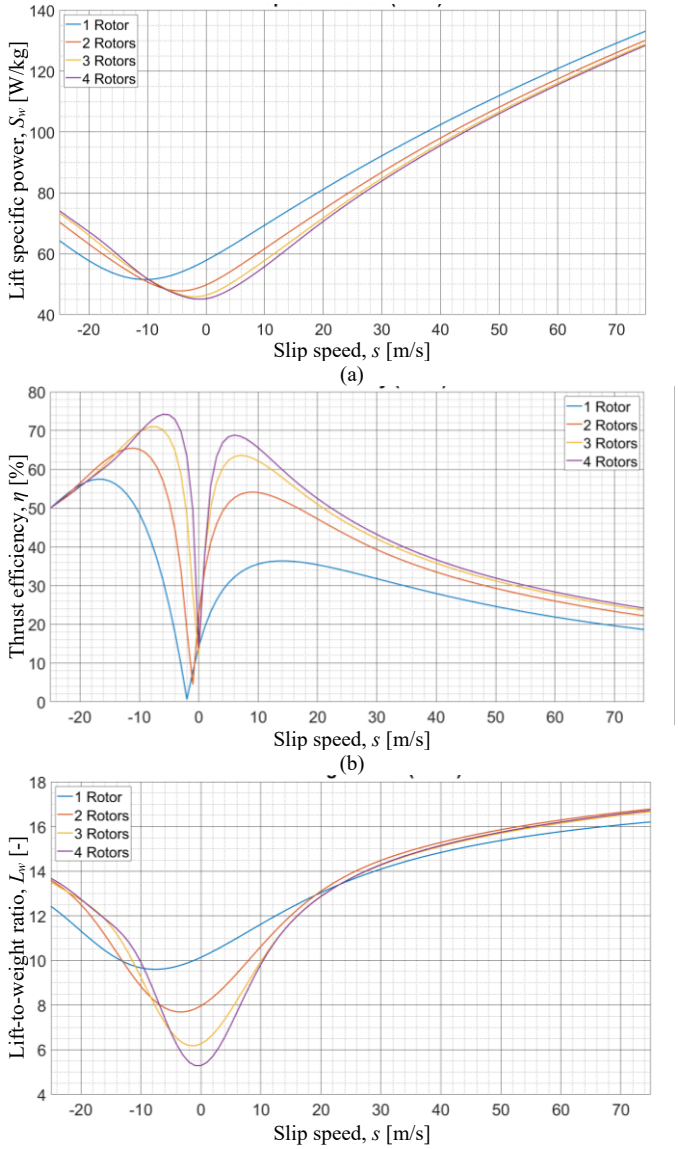

Fig. 21. Example calculation showing the (a) lift specific power, (b) thrust efficiency and (c) lift-to-weight ratio improvements when using multiple rotors in series.

TABLE IV. MULTIPLE ROTOR PARAMETER ANALYSIS

Pole-pairs, P	1	-
Outer radius, r_o	12.7	mm
Inner radius, r_i	3.175	mm
Rotor width	2 r_o	mm
Number of Rotors, n	1,2,3,4	-
Spacing between rotors	r_o	mm
Phase angle between each rotor	[0,180,0,180]	Degrees
Residual flux density, B_{rm}	1.42	T
Relative permeability, μ_r	1.055	-
Translational velocity	25	m/s
Slip	[-25, 75]	m/s
Airgap	10	mm
Track thickness, h	25.4	mm
Track conductivity	5.69×10^7	S/m

REFERENCES

[1] H. Zhang, K. Kails, P. Machura, and M. Mueller, "Conceptual Design of Electrodynamic Wheels Based on HTS Halbach Array Magnets," *IEEE Trans. Applied Superconductivity,* vol. 31, no. 5, pp. 1-6, 2021.

[2] X. Sang *et al.*, "Analysis and Experiment on the Levitation Force and Thrust Force Characteristics of a Permanent Magnet Electrodynamic Wheel for Maglev Car Application," *IEEE Trans. Applied Superconductivity,* vol. 31, no. 8, pp. 1-4, 2021.

[3] J. Bird and T. A. Lipo, "Calculating the forces created by an electrodynamic wheel using a 2D steady-state finite element model," *IEEE Trans. Magn.,* vol. 44, no. 3, pp. 365-372, March 2008.

[4] Z. Zhang *et al.*, "Design and Operating Mode Study of a New Concept Maglev Car Employing Permanent Magnet Electrodynamic Suspension Technology," *Sustainability,* vol. 13, no. 11, p. 5827, 2021.

[5] W. Q. a. J. Z. Bird, "Electrodynamic Wheel Magnetic Rolling Resistance," *IEEE Trans. Magn., vol. 53, no. 8,* vol. 53, no. 8, p. Art no. 8107407, 2017.

[6] J. Wright and J. Z. Bird, "Analytic Damping and Stiffness Analysis for a 4-DOF Electrodynamic Wheel Maglev Vehicle," in *2018 XIII International Conference on Electrical Machines (ICEM)*, 3-6 Sept. 2018 2018, pp. 555-561.

[7] K. S. Jung, "Spatial transfer of conductive plate through decoupling of two axial electrodynamic forces generated by magnet wheel," *Mechatronics,* vol. 23, no. 8, pp. 1044-1050, 2013.
[8] D. Ogawa, Y. Horiuchi, and N. Fujii, "Calculation of electromagnetic forces for magnet wheels," *IEEE Trans. Magn.,* vol. 33, no. 2, pp. 2069-2072, March 1997.
[9] N. Fujii, G. Hayashi, and Y. Sakamoto, "Characteristics of magnetic lift, propulsion and guidance by using magnet wheels with rotating permanent magnets," in *Ind. App. Conf.* Rome, Italy, Oct. 2000, pp. 257-262.
[10] N. Fujii, K. Naotsuka, K. Ogawa, and T. Matsumoto, "Basic characteristics of magnet wheels with rotating permanent magnets," in *Ind. Appl. Conf.*, Denver, CO, USA, 1994, vol. 1, pp. 203-209.
[11] D. G. Henderson *et al.*, "Hoverboard," USA, Jun. 15, 2015.
[12] J. Z. Bird, "A Review of Integrated Propulsion, Suspension and Guidance Passive Guideway Maglev Technologies," in *2019 12th Intern. Symp. Linear Drives for Industry Appl. (LDIA)*, 1-3 July 2019 2019, pp. 1-6.
[13] J. F. Eastham and D. Rodger, "The performance of induction levitators," *IEEE Trans. Magn.,* vol. 20, no. 5, pp. 1684-1686, Sept. 1984.
[14] J. Bird and T. A. Lipo, "Characteristics of an electrodynamic wheel using a 2-D steady-state model," *IEEE Trans. Magn.,* vol. 43, pp. 3395-3405, Aug. 2007.
[15] Y. Yuan *et al.*, "Working Principle and Primary Electromagnetic Characteristics of a Permanent Magnet Electrodynamic Wheel for Maglev Car Application," *IEEE Trans. Applied Superconductivity,* vol. 31, no. 8, pp. 1-5, 2021.
[16] S. Paul, "Three-dimensional steady state and transient eddy current modeling," Ph.D. Thesis, Elect. Comp. Eng., Univ. N.C. at Charlotte, Charlotte,NC, 2014.
[17] S. Paul, W. Bomela, N. Paudel, and J. Z. Bird, "3-D Eddy Current Torque Modeling," *IEEE Trans. Mag.,* vol. 50, no. 2, pp. 905-908, 2014.
[18] N. S. Nise, *Control Systems Engineering*, 2nd Edition ed. Benjamin/Cummings Pub. Co., Inc., 1995.
[19] S. Paul, D. Bobba, N. Paudel, and J. Z. Bird, "Source field modeling in air using magnetic charge sheets," *IEEE Trans. Mag.,* vol. 48, no. 11, pp. 3879-3882, 2012.
[20] S. Paul, W. Bomela, N. Paudel, and J. Z. Bird, "3-D eddy current torque modeling," *IEEE Trans. Magn.,* vol. 50, no. 2, p. 7022404, Feb. 2014.